nature physics

SUPPLEMENTARY INFORMATION

DOI: 10.1038/NPHYS3173

Spatial variation of a giant spin–orbit effect induces electron confinement in graphene on Pb islands

Fabián Calleja, Héctor Ochoa, Manuela Garnica, Sara Barja, Juan Jesús Navarro, Andrés Black, Mikhail M. Otrokov, Evgueni V. Chulkov, Andrés Arnau, Amadeo L. Vázquez de Parga, Francisco Guinea and Rodolfo Miranda

INDEX

DOI: 10.1038/NPHYS3173

A. Experimental

A.1.- Intercalation Process

The Ir(111) surface was prepared by cycles of Ar+ ion sputtering at 1.5 keV and 8 μA current on the sample, and flash annealing to 1400K. After several cycles, the surface was exposed to ethylene at 10^{-7} Torr partial pressure while keeping the sample at 1100K[S1]. This procedure results is an atomically flat Ir(111) surface almost completely covered by a single monolayer of graphene, as shown in Fig. S1a. In addition to the substrate monoatomic steps, some wrinkles of the graphene sheet (long white lines) and some graphene free areas (darker patches) are resolved.

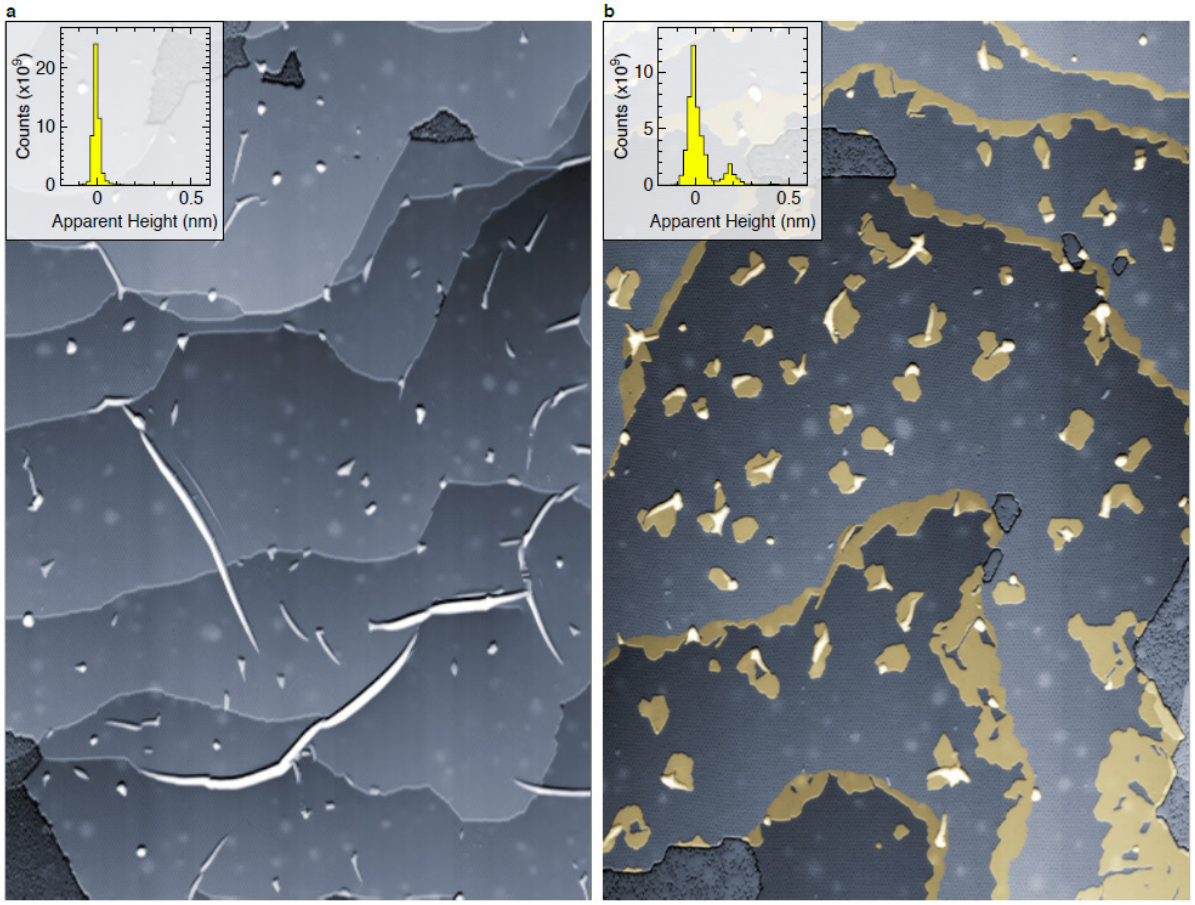

Figure S1 *270 nm x 400 nm STM images acquired on a gr/Ir(111) sample before (**a**)and after (**b**) Pb intercalation. The insets show the apparent height distribution on a single terrace covering an area of the order of 10000 nm^2. The intercalated islands have been highlighted for an easier identification.*

Evaporating of the order of 100 ML of Pb on the gr/Ir(111) sample at 800 K results in Pb intercalation of 20% of the surface, as illustrated in Fig. S1b. Three different intercalation centers can be distinguished: monoatomic steps of the Ir substrate, graphene wrinkles and the edges of the graphene free areas. The inset in Fig. S1b shows that the apparent height of the intercalated regions indicates that they are one Pb atom high. Two main evidences indicate

that Pb is actually intercalated underneath graphene (rather than being deposited on top of it): Atomic resolution images acquired on the Pb-intercalated regions reveal that the graphene's atomic lattice extends continuously across the border towards the neighboring gr/Ir(111) areas (see e.g. Figure 1 in main text). Furthermore, some of the graphene wrinkles that extend over several terraces arising from the gr/Ir(111) preparation procedure disappear upon Pb intercalation, as shown in Fig. S1b. This is due to an in-plane strain relaxation of the graphene sheet driven by the intercalation process[S2].

A.2.- Atomic Structure of the Interlayer

A.2.1.- Pb/Ir(111)

The Ir(111) sample was prepared by several cycles of Ar+ sputtering at 1.5 keV and 8 μA current on the sample and flash annealing to 1400K. The deposition of Pb was carried out by keeping the Ir sample at 800K during the evaporation of an equivalent dose of 20 ML of Pb. The result of this preparation is an almost complete monolayer of Pb/Ir(111), as deduced from our STM images.

Fig. S2 reproduces the LEED pattern recorded on a Ir(111) sample covered with 1 ML of Pb. The corresponding crystallographic structure of the Pb monolayer reflects three domains of a c(4×2) rectangular unit cell of Pb atoms. The Pb and Ir related spots in the LEED pattern of the Pb-intercalated gr/Ir(111) system (see Fig. S3a below) are identical to the ones shown in Fig. S2 proving that the atomic arrangement of the Pb monolayer directly adsorbed on Ir(111) is identical to the one observed for the Pb-intercalated gr/Ir(111) system (shown in Fig. 1d). In the intercalated system, the graphene overlayer can, thus, be considerd as residing on top of an undisturbed c(4×2) monolayer of Pb on the Ir surface.

DOI: 10.1038/NPHYS3173

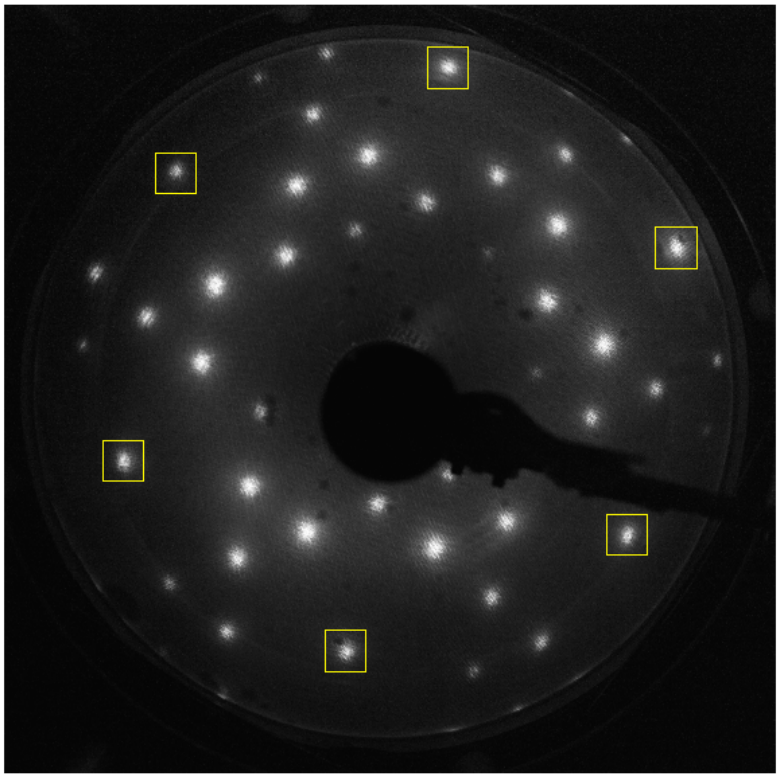

Figure S2 *Low Energy Electron Diffraction (LEED) pattern acquired for a ML of Pb deposited on Ir(111). The Ir related spots are framed in yellow. The Pb-derived spots form a c(4x2) rectangular structure identical to the one observed from the Pb-intercalated gr/Ir(111) sample.*

A.2.2.- gr/Pb/Ir(111)

Fig. S3a shows the LEED pattern obtained from a Pb-intercalated gr/Ir(111) sample with 80% of the surface intercalated by Pb. The LEED pattern presents the first order diffraction spots of the graphene and Ir lattices (marked with grey and black squares respectively), as well as the extra spots related to the lattice of Pb (marked with coloured circles). These extra spots can be divided into three groups arising from three rotational domains (in red, green and blue respectively), each one corresponding to a rectangular c(4×2) Pb superstructure commensurated with the Ir lattice. This structure is identical to the one obtained by deposting directly Pb on a clean Ir(111) surface.

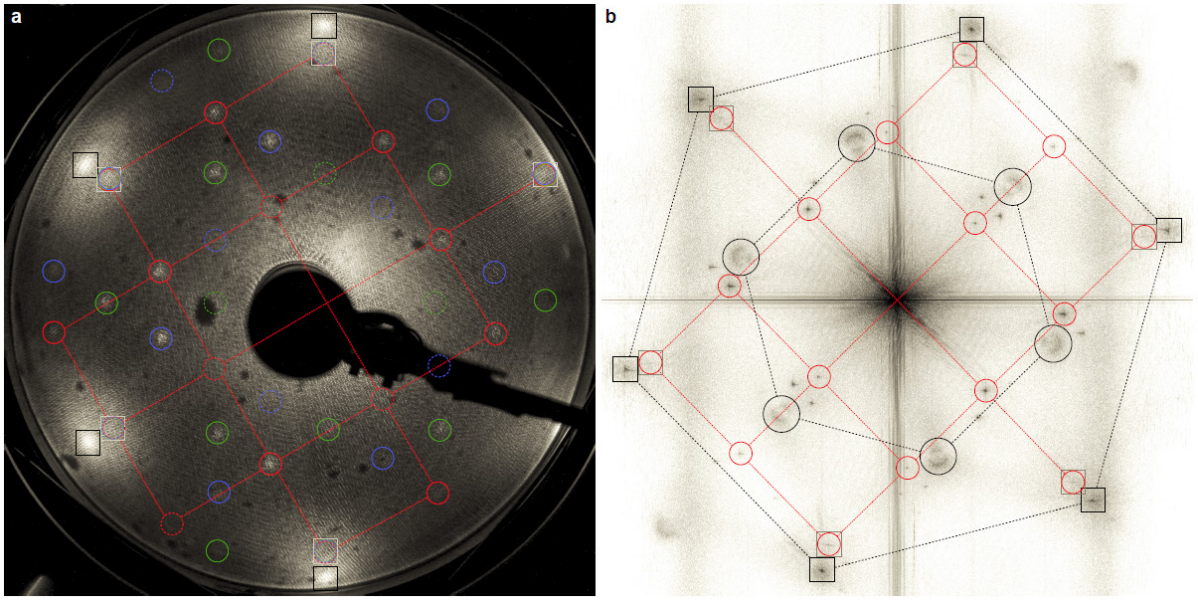

Figure S3 a, *LEED pattern from an 80% intercalated gr/Pb/Ir(111) surface. Black and grey squares indicate graphene and Ir spots, respectively. Red green and blue circles mark Pb spots from each one of the three rotational domains, respectively;* ***b,*** *Fourier Transform of a low voltage STM image acquired on a single domain island of a 20% intercalated gr/Pb/Ir(111) sample. Black and grey squares signal graphene and Ir spots respectively. The single domain, Pb-derived spots are highlighted in red circles. The inner black circles mark the corners of the surface Brillouin Zone, where intervalley scattering rings appear. Notice that the Pb spots are commensurate with the ones coming from Ir.*

The structural arrangement of the Pb-intercalated islands observed in Fig. 1 of the main text is identical to the one of the fully (80%) intercalated sample. This is confirmed in Figure S3b, which shows a Fast Fourier Transfer (FFT) map obtained from an STM image acquired on a gr/Pb/Ir island displaying a single domain. Graphene and Ir spots are marked with grey and black squares, respectively and Pb spots are marked with red circles. The additional spots can be associated to the moiré structure of the gr/Ir interface[S1]. In agreement with the LEED analysis, the resulting Pb-related rectangular structure is commensurated with the Ir lattice. This structure is translated to real space in the model presented in Fig. 1c of the main text. Notice that our LEED-STM analysis does not allow to determine the lateral position of the Pb lattice. Our election of placing the Pb atoms exactly at threefold positions of the Ir lattice is arbitrary.

A.2.3.- Intervalley scattering and Dirac point

The FFT map of Figure S3b presents additional circular features at the corners of the surface Brillouin zone (indicated by black circles), due to inter-valley scattering between

DOI: 10.1038/NPHYS3173

neighbouring Dirac cones[S1]. Furthermore, since the source STM image was acquired at a very small bias voltage (3 mV), the observed scattering signatures can be related to the LDOS at the Fermi level. Normalising graphene's lattice parameter to its freestanding value, we obtain a measured ring radius of $2q_F$=0.36±0.04 nm^{-1}. Assuming the Fermi velocity of freestanding graphene, this leads to an estimated Dirac point of ±110±20 meV for gr/Pb/Ir (the indetermination in the sign of the doping comes from the fact that we probed only the Fermi level). Additionally, the anisotropy in the intensity of the inter-valley rings indicates that the graphene's sub-lattice symmetry is preserved during the intercalation process[S3]. This is consistent with the proposed Pb structure, which is incommensurate with the graphene overlayer and does not break its symmetry.

A.2.4.- Three rotational domains of gr/Pb/Ir(111)

One of the implications of the proposed structure is the existence of three possible rotational domains, arising from the combination of the hexagonal and rectangular lattices of graphene and Pb, respectively. The three domains, clearly present in the LEED pattern of Fig. S3a, were also resolved by STM. This was achieved by lowering slightly the deposition temperature, so that the average domain size was small enough to capture several domains on a single STM image with atomic resolution, as the one shown in Fig. S4. This image shows a 50 nm wide intercalated region contained in a single atomic terrace of the substrate, where the dark patches correspond to small non intercalated gr/Ir areas. The three domains have been labelled d1, d2 and d3 respectively, and shadowed lines have been added as a visual guide to mark the domain boundaries. The increased defect density as compared to the image shown in Fig. 1 of main text is a side effect of the low deposition temperature. The insets at the right of Fig. S4 are the FFT maps (in inverted grayscale) obtained by masking the areas corresponding to each domain in the STM image on the left. In the maps the reciprocal lattices of graphene (blue) and Pb (red) are resolved, displaying their three possible relative orientations.

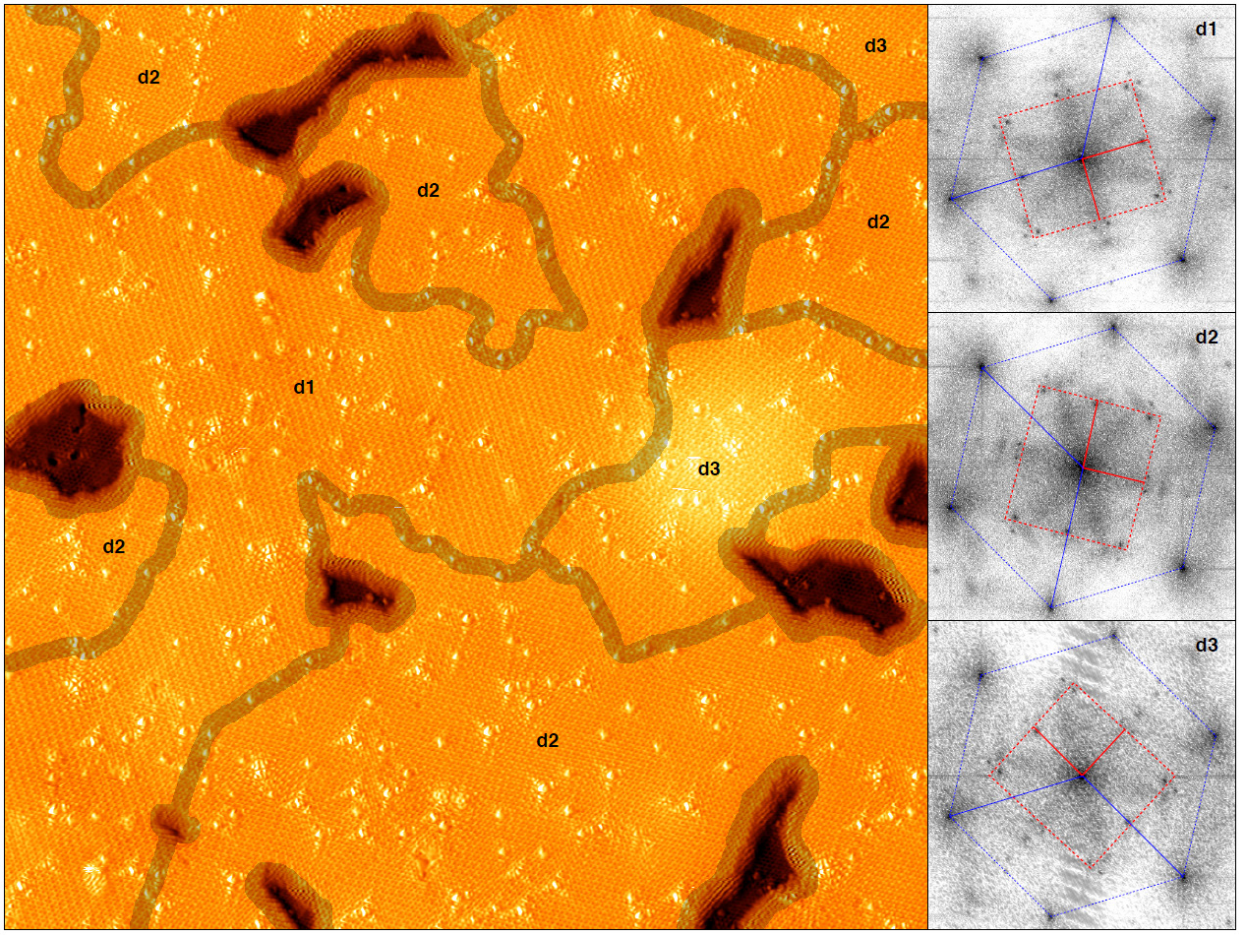

Figure S4 *STM image (50 nm x50 nm) acquired on gr/Pb/Ir(111) prepared at a slightly lower deposition temperature. The dark patches are free (without intercalated Pb) gr/Ir areas, and the shadowed lines are visual guides to separate the three rotational domains (labelled d1, d2 and d3 respectively). The insets at the right are the FFT maps corresponding to each domain, where the reciprocal lattices of graphene and Pb have been highlighted in blue and red, respectively.*

A.3.- STS measurements on islands of different size

All STS spectra (including those in figures 3 and 4 on main text) were acquired by means of lock-in detection, using a modulation of 10mV rms, a time constant of 30 ms and an integration time per point of 50 ms. Since the total number of points was 300, the time per spectrum was close to 15 seconds. Figure S5 compares differential tunnelling conductance spectra recorded in the same conditions on small Pb-intercalated graphene islands of different average size, and on extended gr/Pb/Ir(111) and gr/ Ir(111) regions. The energy separation between pseudo Landau levels scale inversely with the size of the island, while on the larger island (50 nm), the spectrum does not show the pseudo Landau levels and reflect only the electronic structure of graphene on a complete layer of Pb. The spectrum on gr/Ir(111) is also essentially featureless, except for the Dirac points of the moiré superlattice.

DOI: 10.1038/NPHYS3173

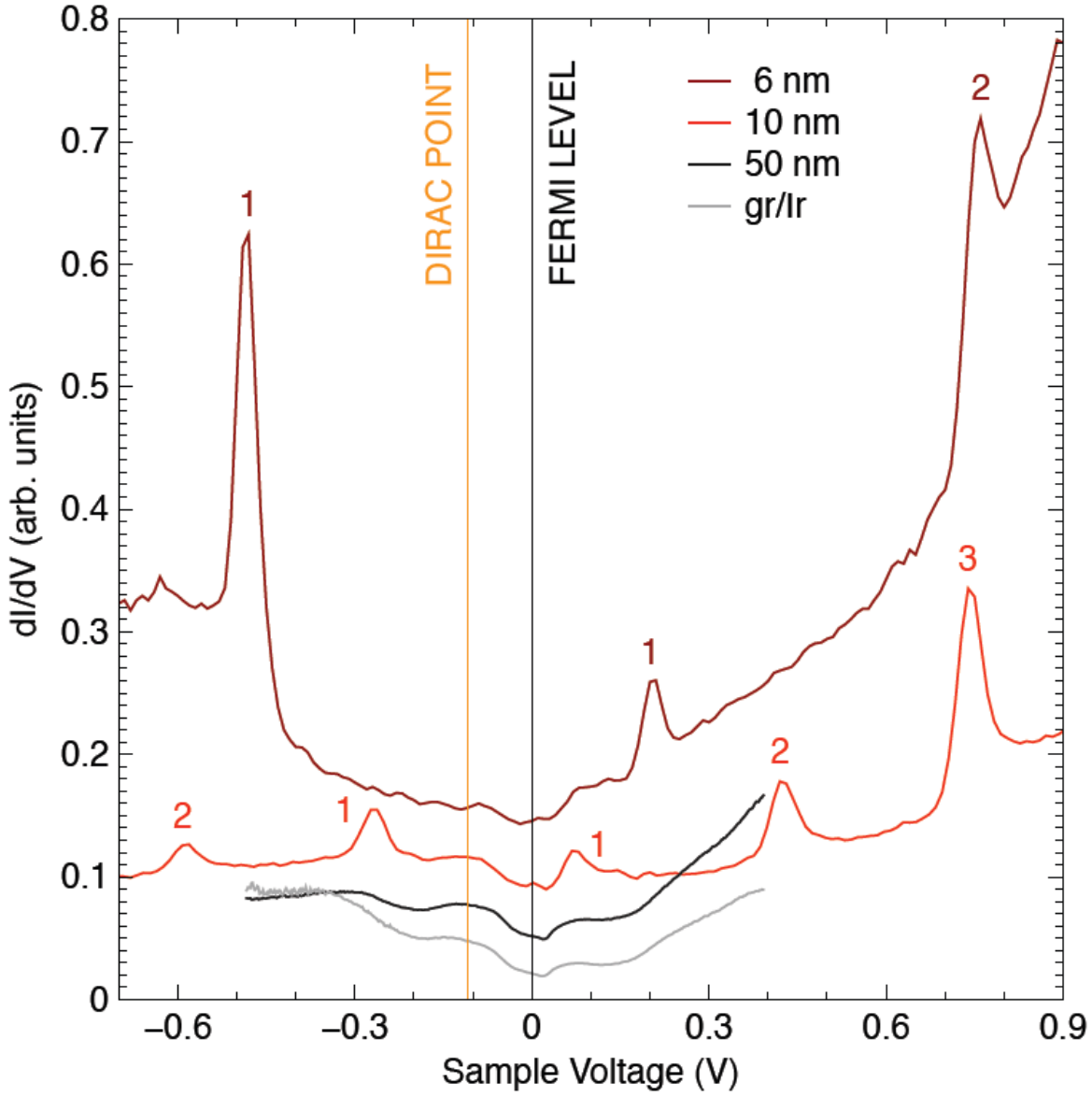

Figure S5 *From above to below, differential conductance (STS) spectra recorded at 4.6 K on the centre of 6, 10 and 50 nm wide gr/Pb/Ir(111) islands. A reference spectrum recorded on gr/Ir(111) is displayed in grey. The Fermi level and Dirac point are marked in black and orange, respectively. The tunnelling gap was stabilized at -1.5 V and 50 pA. Notice the appearance of sharp pseudo Landau levels in the smaller Pb-intercalated islands, with their separation depending on the size of the island and the broad, weaker features associated to the Dirac points of the moiré superlattice in the larger island and in gr/Ir(111). The numbers indicate the assigned quantum numbers, as described in the main text. The spectra have been displaced vertically for clarity.*

B. Theoretical model

B.1- DFT calculations for Pb/graphene: Spin Orbit Coupling

In order to check the existence of sizeable spin-orbit splitting in the π bands of graphene induced by the interaction with Pb, we have performed first-principles Density Functional Theory (DFT) calculations [see also section B.3 Methods] for gr/Pb model systems that capture the essential features of the one experimentally observed.[S3] Specifically, we have used a commensurate 2×2 rectangular arrangement of Pb atoms centered at hollow sites of the graphene honeycomb lattice, located at different vertical distances. This arrangement is practically equivalent to a Pb monolayer in a c(4×2) arrangement with respect to the Ir(111) lattice. In figure S6 we show the DFT band structure for two representative examples of large and short vertical distances between the graphene plane and the Pb layer.

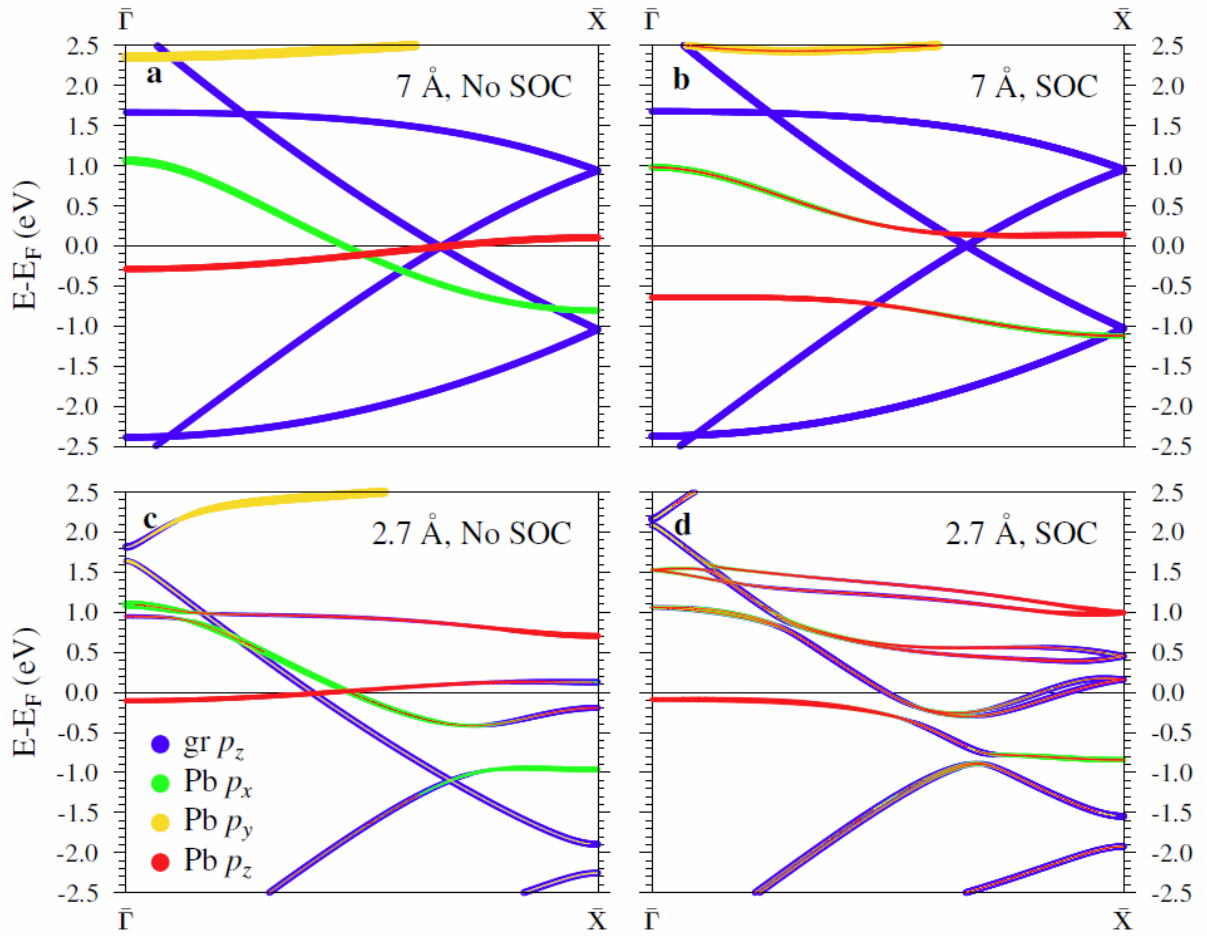

Figure S6 *Band structure along the Γ-X direction for a 2×2 array of Pb atoms at two different vertical distances from the graphene layer of 7Å (upper panels) and 2.7Å (lower panels) in two different approximations: without Spin-Orbit Coupling (left panels) and with Spin-Orbit Coupling (right panels). The orbital character of the bands is shown with different colours for C(p_z) [blue], Pb(p_x) [green], Pb(p_y) [yellow] and Pb(p_z) [red].*

DOI: 10.1038/NPHYS3173

As expected, the results shown in Fig S6 indicate that when the Pb and graphene layers are far away from each other and Spin-Orbit Coupling (SOC) is not included, the resulting bands are simply the superposition of the graphene π bands and the Pb bands with well-defined p-character (p_x, p_y and p_z). Turning on SOC results in a mixing of p_x and p_z Pb derived bands that exchange character as we go from the Γ to the X point of the rectangular supercell Brillouin zone due to the avoided crossing that appears between them as a result of spin-orbit interaction, while the π bands of graphene are not affected by SOC effects. These latter shows the Dirac point at a distance of 2/3 from the Γ point along the Γ-X direction due to band folding.

However, when the distance between the Pb and graphene layers is reduced to 2.7Å, we observe clearly two effects: (i) already in the absence of SOC, there is a strong hybridization between the graphene π bands and the Pb derived bands with p_x and p_z character, and (ii) a rather large spin-orbit splitting of the graphene π bands close to the Fermi level that amounts 109 meV. This result is consistent with previous DFT calculations for a 4x4 array of Pb monomers located at single vacancies in graphene [S4], which reveal a giant enhancement of the SOC with a valence band splitting at the K point as large as 116.6 meV and the opening of a gap. Similar results have been obtained for a 2×2 array of Au atoms adsorbed on graphene [S3].

B.2.- Tight-binding model and phenomenological Hamiltonian

The electronic spectrum deduced from first principles methods can be understood with a relatively simple tight-binding model. This description starts with the usual Hamiltonian for π electrons of graphene including hoppings up to second nearest neighbours:

$$H_{Gr} = \epsilon_0 \sum_i \left(a_i^\dagger a_i + b_i^\dagger b_i\right) - t \sum_{\langle ij \rangle} a_i^\dagger b_j - t' \sum_{\langle\langle ij \rangle\rangle} \left(a_i^\dagger a_j + b_i^\dagger b_j\right) + H.C.$$

For the Pb monolayer, we consider the 4 outer shell electrons in s, p_x, p_y, and p_z orbitals and hoppings between first nearest neighbours in both *x* and *y* directions, parameterized by two-center Slater-Koster parameters, see Table S1. The Spin-Orbit Coupling is introduced only in the subspace of Pb orbitals. We write:

$$H_{SO} = \Delta_{SO}\mathbf{L}\cdot\mathbf{S} = \frac{\Delta_{SO}}{2}\begin{pmatrix} 0 & -i & 0 & 0 & 0 & 1 \\ i & 0 & 0 & 0 & 0 & -i \\ 0 & 0 & 0 & -1 & i & 0 \\ 0 & 0 & -1 & 0 & i & 0 \\ 0 & 0 & -i & -i & 0 & 0 \\ 1 & i & 0 & 0 & 0 & 0 \end{pmatrix},$$

where the matrix acts on the mono-electronic basis $(p_x\uparrow, p_y\uparrow, p_z\uparrow, p_x\downarrow, p_y\downarrow, p_z\downarrow)$.

TB parameters (eV)	ϵ_0	t	t'	ϵ_s	ϵ_{px}	ϵ_{pz}	$V_{sp\sigma x}$	$V_{pp\sigma x}$	$V_{pp\sigma y}$	$V_{pp\pi x}$	$V_{pp\pi y}$	Δ_{SO}	t_x	t_z
7 *Å*	0.9	2.7	-0.3	5.9	1.65	1.38	0.55	0.45	0.4	-0.1	-0.8	0.9	0	0
2.7 *Å*	0.3	2.7	-0.3	5.9	1.95	1.38	0.55	0.45	0.4	-0.1	-0.8	0.9	0.38	0.8

Table S1: *Tight-binding parameters employed in the calculation.*

As shown in Fig. S7, this model reproduces well the DFT bands when the distance between the Pb adlayer and graphene is 7 Å. For smaller distances the graphene bands start to hybridize with the Pb bands. We introduce hoppings between $p_{x,y}$ and p_z orbitals of Pb and the 6 neighboring carbon atoms of graphene parameterized by t_x and t_z respectively. The bands corresponding to a distance of 2.7 Å with SOC are shown in Fig. S8, where the right panel shows a zoom of the lowest energy bands dominated by the graphene Dirac point strongly hybridized with one of the Pb bands. The spin-orbit interaction within the Pb bands is clearly transferred to graphene bands, in this case by opening a Kane-Mele gap of the order of 600 meV.

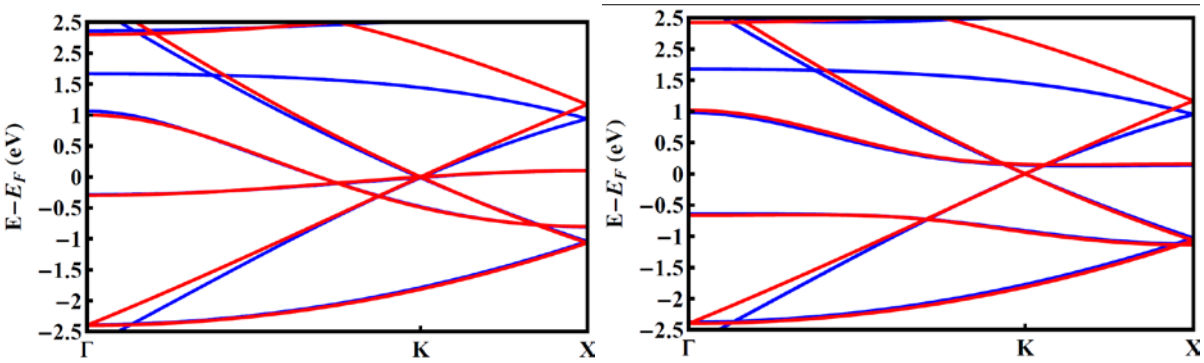

Figure S7: *DFT (in blue) and tight-binding (in red) band structure calculation for a distance between graphene and the Pb adatoms of 7 Å, with (right) and without (left) spin-orbit coupling. The tight-binding parameters are summarized in Table S1.*

Note that the generation of a Kane-Mele coupling is favoured by the fact that the Pb atoms in the calculation are assumed to occupy the central positions of graphene hexagons. This does not correspond to the situation of the experiments, where the Pb monolayer is

DOI: 10.1038/NPHYS3173

incommensurate with graphene. In order to reproduce the experimental situation, we construct an effective Hamiltonian based on group theory arguments, which reproduces the spin-orbit features of graphene bands in the situation considered in the microscopic calculation.

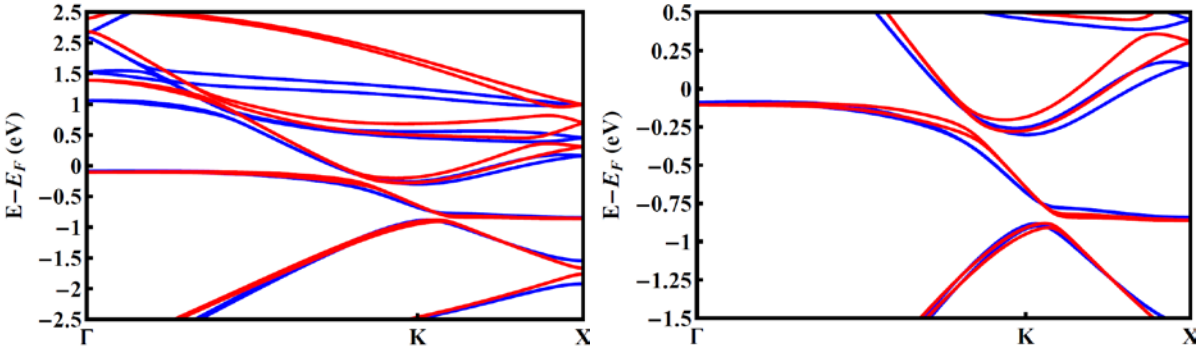

Figure S8: *DFT (in blue) and tight-binding (in red) band structure calculation for a distance between graphene and the Pb adatoms of 2.7 Å, with spin-orbit coupling. The right panel zooms into the Dirac point region. The tight-binding parameters are summarized in Table S1.*

Generically speaking, superlattice perturbations couple to graphene π electrons as scalar and gauge potentials. According to our DFT and tight-binding calculations described above, we assume that the Pb sublayer induces a strong Spin-Orbit Coupling in graphene, similarly to the case of heavy adatoms[S5]. The superlattice formed by the presence of Pb creates spin-dependent potentials. Since the mirror symmetry of the graphene crystal is broken, such potentials contain in general the in-plane spin operators S_x, S_y. The form of such potentials can be deduced from group theory arguments. The point group of graphene on an incommensurate substrate is the intersection of the original hexagonal group C_{6v} with the point group of the substrate. In this case, being interested only on the effect of Pb, and given that Pb atoms form a rectangular lattice, we conclude that the symmetry group of the substrate is orthorhombic, C_{2v}, which is a subgroup of C_{6v}. Therefore, only the symmetry operations of the original group contained in C_{2v} survive. Those are the C_2 rotation about the axis orthogonal to the graphene plane and inversion operations about the vertical planes defined by the dashed and dotted lines in Fig. S9.

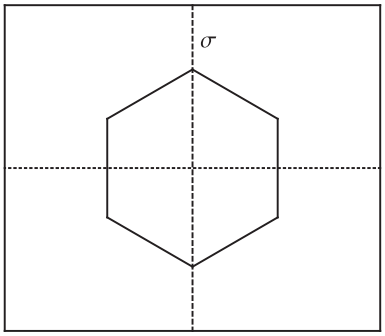

Figure S9: *Unit cells of the hexagonal (C_{6v}) graphene lattice and the rectangular (orthorhombic, C_{2v}) substrate of Pb atoms.*

The electronic operators can be classified according to the irreducible representations of C_{2v} as shown in Table S2. Only complete scalars (~A_1) which are even under time reversal symmetry may appear in the Hamiltonian. Such combinations are σ_x, $\tau_z\sigma_z S_z$, $\tau_z S_y$, $\tau_z\sigma_x S_y$, and $\sigma_y S_x$, where σ_i, τ_i are Pauli matrices associated to sublattice and valley degrees of freedom respectively.

Irrep	*T* even	*T* odd
A_1	σ_x	-
A_2	-	s_z
B_1	-	τ_z, s_y
B_2	σ_z	σ_y, s_x

Table S2: *Classification of electronic operators according to the irreducible representations of C_{2v} and time reversal (T) operation.*

This can be checked straightforwardly by considering the unitary operators that implement the symmetry operations of C_{2v} and time inversion in the Hilbert space of the Bloch wave functions at the $\pm\mathbf{K}$ points. Note that the orbital part of the wave function is a vector of the form $\Psi = (\psi_{A+}, \psi_{B+}, \psi_{A-}, \psi_{B-})^T$ belonging to a 4-dimensional reducible representation of C_{2v} that we denote by G, where each entry $\psi_{A/B\pm}$ represents the amplitude of the wave function on sublattice A/B at valley $\pm\mathbf{K}$. The matrices of such representation in this basis are:

$$C_2\colon\ \tau_x\sigma_x$$
$$\sigma_v\colon\ \sigma_x$$
$$\sigma_v'\colon\ \tau_x$$
$$T\colon\ \tau_x K$$

Here T is time inversion and K is complex conjugation. Note that the operators of C_2, σ_v, and σ_v' operations commute with each other since C_{2v} is abelian. With this and the character table

DOI: 10.1038/NPHYS3173

of the group we classify valley diagonal operators $\sigma_{x,y,z}$ and τ_z according to the irreducible representations of C_{2v} as indicated in Table S2.

Irreps of C_{2v} Double group	E	$\bar{E}$	$2C_2$	$2\sigma_v$	$2\sigma_v'$
A_1	1	1	1	1	1
A_2	1	1	1	-1	-1
B_1	1	1	-1	1	-1
B_2	1	1	-1	-1	1
$D_{1/2}$	2	-2	0	0	0

Table S3: *Character table for C_{2v} double group.*

The spinorial part of the wave function transforms according to the 2-dimensional irreducible representation $D_{1/2}$ of the C_{2v} double group, check the character table in Table S3. In such representation the symmetry operations read:

$$C_2\colon\ i\,s_z$$
$$\sigma_v\colon\ s_y$$
$$\sigma_v'\colon\ s_x$$
$$T\colon\ i\,s_y K$$

The transformation properties of s_i matrices are trivially inferred from the reduction

$$D_{1/2}\ \times\ D_{1/2} \sim A_1 + A_2 + B_1 + B_2,$$

or equivalently from the transformation of s_i matrices under the operations of C_{2v} double group in the $D_{1/2}$ representation. Note that now these operators do not commute with each other because the double group is no longer abelian. Then, one may form invariants using Tables S2 and S3, obtaining, apart from the Kane-Mele coupling, the following spin-orbit coupling terms:

$$\tau_z s_y$$
$$\tau_z \sigma_x s_y$$
$$\sigma_y s_x$$

Such terms transforms trivially under the matrices of the $G\ \times\ D_{1/2}$ representation:

$$C_2\colon\ i\,\tau_x\sigma_x s_z$$
$$\sigma_v\colon\ \sigma_x s_y$$
$$\sigma_v'\colon\ \tau_x s_x$$
$$T\colon\ i\,\tau_x s_y K$$

Thus, the phenomenological Hamiltonian valid around the Brillouin zone corners $\pm\mathbf{K}$ read in general:

$$H = v_F \boldsymbol{\Sigma} \cdot (-i\nabla + \boldsymbol{A}) + \beta t \sigma_x \pm \Delta_{KM} \sigma_z s_z \pm A_0 s_y$$

where $\boldsymbol{\Sigma} = (\pm\sigma_x, \sigma_y)$, $\boldsymbol{A} = (A_x s_y, A_y s_x)$, and $\pm$ holds for valleys $\pm\mathbf{K}$. The bands deduced from this model for $\beta = -0.025$, $\Delta_{KM} = 0.3$ eV and $A_x = A_y = A_0 = 0.02$ eV are shown in Fig. S10.

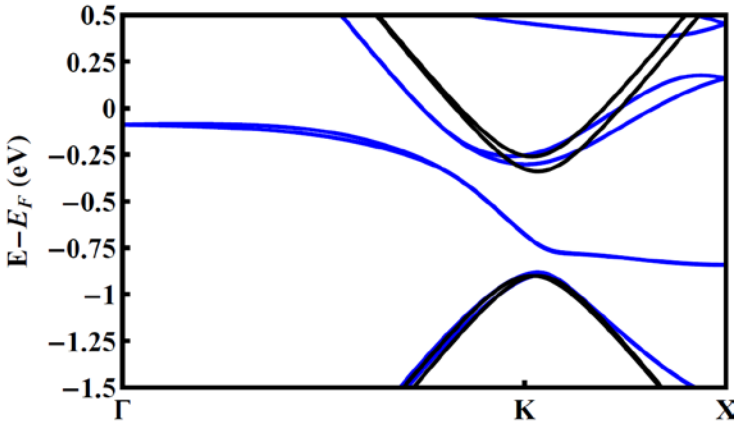

Figure S10: *DFT (in blue) calculated bands compared with the phenomenological Dirac equation (in black).*

In the incommensurate situation the Kane-Mele coupling is expected to be strongly suppressed. Similarly, we neglect the coupling β, so the previous Hamiltonian reduces to the one discussed through the main text. At this level, the remaining fields $A_{0,x,y}$ are phenomenological constants associated to the three independent spin-orbit coupling terms that we have constructed with group theory arguments. These fields can be interpreted as the components of non-abelian gauge fields since in general $[\boldsymbol{A}_i, \boldsymbol{A}_j] \neq 0$. This situation is formally identical to the one in the context of twisted bilayer grapheme[S6], where the inter-layer couplings can be also interpreted as components of non-abelian gauge fields, but in that case the additional internal degrees of freedom is the layer instead of the spin. As in that case, a non-uniform spatial dependence of these fields could lead to electronic confinement.

DOI: 10.1038/NPHYS3173

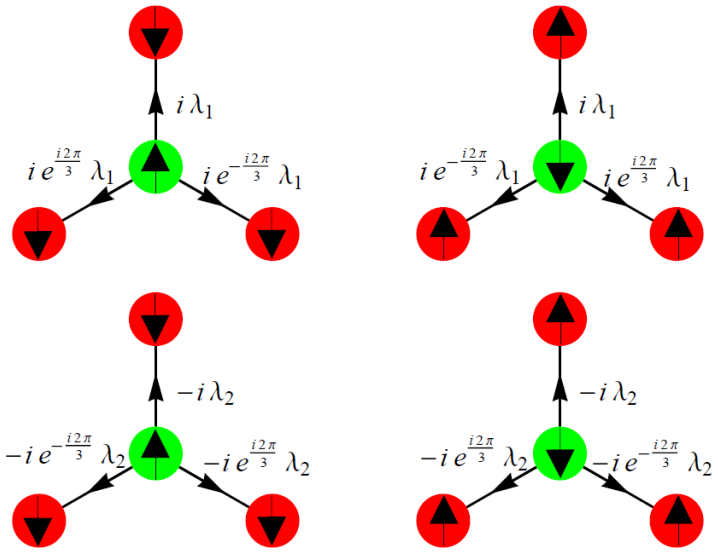

Figure S11: *Hopping terms leading to* ***A*** *at the* $\pm\mathbf{K}$ *points.*

In order to simulate this phenomenological Hamiltonian we consider the usual tight-binding description of graphene in terms of first-neighbors hopping t between π orbitals, then $v_F = 3ta/2$. The spin-orbit couplings are introduced by considering the suitable spin-flip hopping terms. The first neighbors complex hopping terms shown in Fig. S11 generate the gauge field $\boldsymbol{A}$. Similarly, the field A_0 is related to the spin flipping hopping between second nearest neighbors illustrated in Fig. S12. We have:

$$A_0 = 3\sqrt{3}\lambda_0$$

$$A_x = \frac{\lambda_1 + \lambda_2}{ta}$$

$$A_y = \frac{\lambda_1 - \lambda_2}{ta}$$

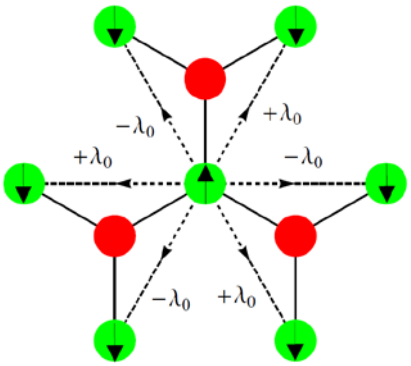

Fig. S12: *Hopping terms leading to* A_0 *at the* $\pm\mathbf{K}$ *points.*

B.2.- Methods and results

Density Functional Theory (DFT) calculations

The DFT calculations were performed using the VASP code[S7] within the projector augmented wave method[S8] to treat ion-electron interactions. The generalized gradient approximation to exchange and correlation in the Perdew-Burke-Ernzernhof version [S9] was used. The Hamiltonian contained the scalar relativistic corrections and the spin-orbit coupling was taken into account by the second variation method [S10]. The energy cut-off in the plane wave expansion was 600 eV. Convergency with respect to the k-point sampling was achieved using a Monkhorst pack grid of 12×12×1 k-points. For the band structure calculations we used 600 k-points along the Γ-X direction of the supercell Brillouin zone, in which the original zone boundary point K appears at 1/3 Γ-X distance of the zone boundary point X of the rectangular supercell Brillouin zone due to band folding. The rectangular supercell is $2*a_0$ and $\sqrt{3}*a_0$ large in size along the X and Y directions, respectively, being a_0=2.46 Å the graphene lattice constant of the honeycomb lattice and, therefore, it contains one Pb and eight carbon atoms in the unit cell. In the vertical Z-axis, a minimum distance of 10 Å between periodic replicas of the slab were used, but it was extended up to 20 Å, so that we could treat also large Pb-graphene distances without spurious effects, something that required a large number of plane waves.

Spatial variation of the SOC

In the phenomenological model the transition from gr/Ir to gr/Pb/Ir is modeled as a region where the spin-orbit coupling changes from zero to a certain finite value. For simplicity, we assume that the spin-orbit coupling changes in the armchair direction (*y* axis in the previous analysis). Translation invariance in the direction along the border between the two regions is assumed, so the crystalline momentum (*k*) along the zig-zag direction is conserved. For each *k*, the problem can be mapped to a generalized tight-binding chain with two atoms per unit cell with *k*-dependent inter-cell hopping terms, see Fig. S13.

We compute the retarded Green function at the sites of the chain where the spin-orbit coupling changes. The region where the spin-orbit changes are modeled as a finite chain connected to semi-infinite leads where the spin-orbit is taken as a constant. The effect of the leads is incorporated as a self-energy, which is computed from the Dyson equation for the leads. Then, the Green operator for the chain is calculated, and from this we have the local density of states (LDOS) for each *k*. Finally we integrate in *k*.

DOI: 10.1038/NPHYS3173

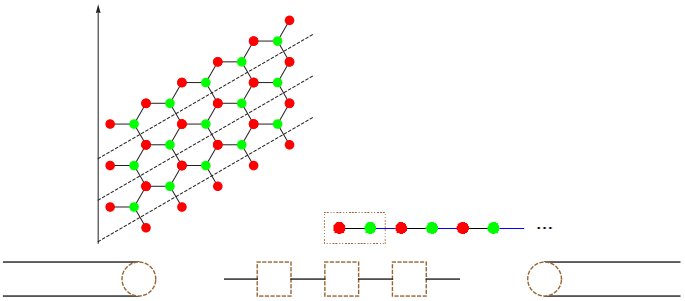

Figure S13: *Translation invariance in the zig-zag direction is assumed. The problem for each k can be mapped to a 1 dimensional tight-binding chain with 2 atoms per unit cell, where the (complex) hopping between cells (in blue) depends on k expressively. A finite chain (the region where the spin-orbit changes) is connected to two semi-infinite leads (where the spin-orbit is taken as a constant). The effect of the semi-infinite leads is incorporated to the Green operator of the chain by means of a certain self-energy, which is computed from the solution of the Dyson equation for the leads.*

The results when only the gauge potential ***A*** is included are shown in Fig. S14. We assume a spatial profile for $\lambda_{1,2}$ as the one shown in Fig. 4a of the main text. The LDOS develops peaks for considerable strong spin-orbit couplings (maximum values), $\lambda_{1,2} \gtrsim 0.1\,t$. In the case of $\lambda_1 \sim \lambda_2$, the spectrum resembles the one of Landau levels due to a real magnetic field applied to graphene.

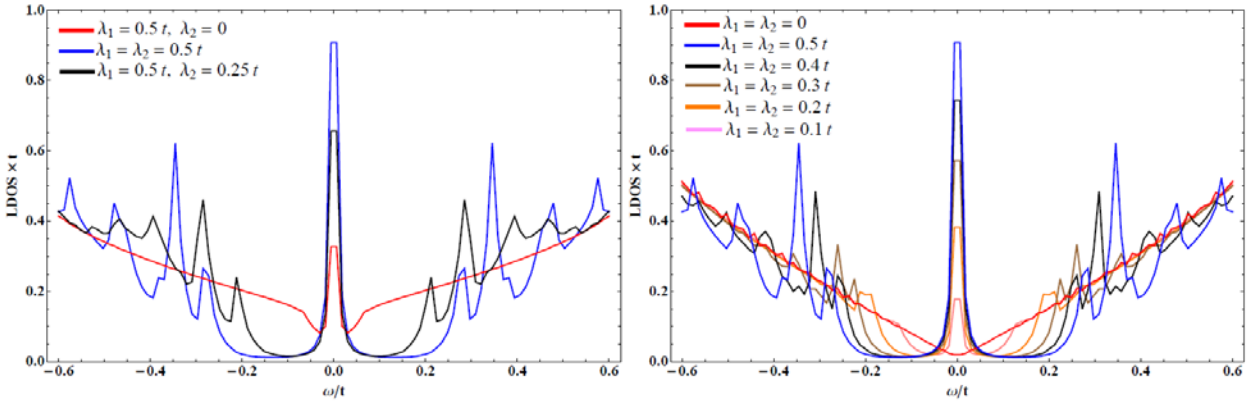

Figure S14: *LDOS when only the gauge potential **A** is considered.*

In order to obtain a sequence of peaks qualitatively more similar to the ones obtained in the experiments we must include the scalar potential A_0. The calculation shown in Fig 4b of the main text corresponds to a *uniform* scalar potential of $\lambda_0 = 0.02\,t$. If we assume for λ_0 the same spatially varying profile as for $\lambda_{1,2}$, the result, as shown in Fig. S15, is similar (compare to Fig. 4b).

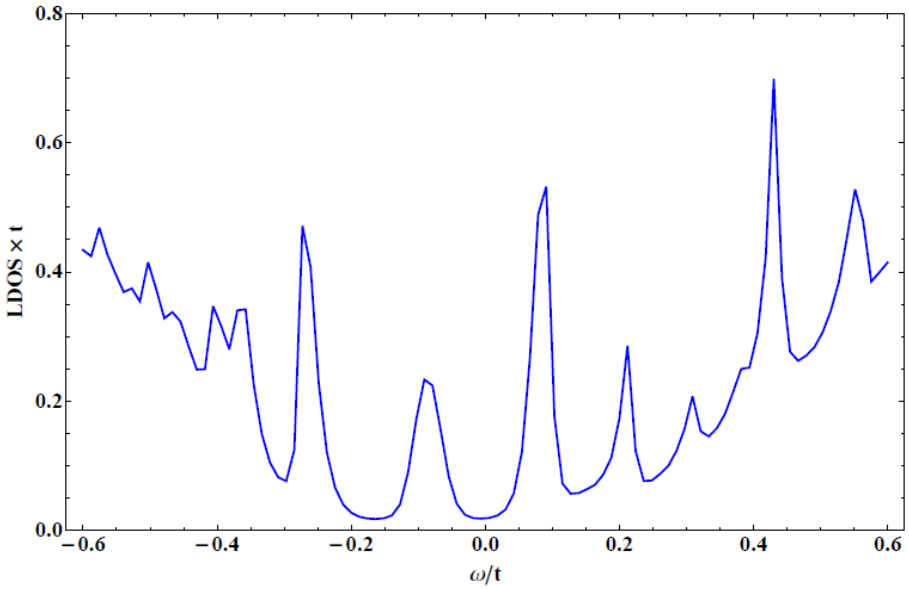

Figure S15: *LDOS when both the gauge* ***A*** *and scalar* A_0 *potentials are considered. The spatial profile is the same in both cases. The maximum values of the couplings are* $\lambda_{1,2} = 0.5\ t$, $\lambda_0 = 0.02\ t$.

B.3.- Topological aspects

According to the tight-binding calculation, the peaks are clearer when λ_1 and λ_2 are of the same order, and they seem to follow the same sequence as the Landau levels of the Dirac Hamiltonian. Consider the previous Hamiltonian. If we set $\lambda_1 = \lambda_2 = \lambda(y)$, the components of the gauge field reduce to $A_x = 2\lambda(y)/ta$ and $A_y = 0$. Note that this field, under a U(2) (global) transformation of the form $U = \exp\left[i\frac{\pi}{4}I - i\frac{\pi}{3\sqrt{3}}\sum_i s_i\right]$, it is equivalent to an abelian gauge field with opposite sign for each spin component.

Therefore, under this U(2) transformation the phenomenological Hamiltonian is mapped to two copies of the Dirac equation in the presence of an out-of-plane magnetic field with opposite sign for each spin projection. This situation resembles the quantum valley hall state proposed in graphene, where strain generates pseudo-magnetic fields with opposite sign at each valley[S11], but in this case the valley degree of freedom is replaced by spin. Moreover, the present model consists of two copies of the quantum spin hall state proposed by Bernevig and Zhang[S12]. Thus, surrounding Pb regions we expect a situation qualitatively similar to the one depicted in the inset of Fig. 4 of the main text. The Pb islands induce a strong spin-orbit coupling in graphene, which decays as we get away from the islands. Surrounding the region where the spin-orbit coupling changes, symbolized by the colour gradient, we expect spin-

DOI: 10.1038/NPHYS3173

polarized counter-propagating edge states. Note that the spin polarization is in-plane, which makes these spin currents more difficult to be detected.

Interestingly, the scalar field separates in energy the sequence of Landau peaks associated to each Kramers pair for which the system is a $\mathbb{Z}_2$ topological insulator[S13]. This energy separation allows populating an odd number of Landau levels. In that situation, an odd number of Kramers pairs of edge modes cross the Fermi level, and therefore, at least one pair of the counter propagating edge channels is topologically protected against disorder by time-reversal symmetry. The characteristic decay length of these modes into the region where the spin-orbit changes goes like $\ell \sim 3ta/\sqrt{2}\Delta$, where Δ is the energy separation between pseudo-Landau levels. From the experiments we have roughly$\Delta = 0.1\,t$, so we expect $\ell \sim 20\,a$, which is less than the characteristic length ($\sim 60\,a$) over which the spin-orbit changes in the numerical calculation.

Finally, the robustness of this picture is discussed, since in the previous dissertation $\lambda_1 = \lambda_2$ is assumed. If $\lambda_1 \neq \lambda_2$ then we have a non-zero y component of the gauge field. This component can be gauged away by a local U(2) transformation of the form $U(y) = e^{i\int_0^y d\zeta\, A_y(\zeta) s_x}$. This makes the x component to oscillate in spin space during the characteristic length $\mathcal{L} = \pi ta/\langle\lambda_1 - \lambda_2\rangle$, where the brackets denote the mean value. The precession in spin space is the manifestation of the non-abelian nature of the gauge field. The problem is no longer equivalent to two copies of the Dirac equation in the presence of a magnetic field with opposite sign for each spin projection. Nevertheless, for slow precession, $\ell/\mathcal{L} \ll 1$, the Landau levels are expected to survive, as shown in the numerical calculation. Given that the Landau gaps remain open the survival of the topological properties of the system are guaranteed.

References:

S1 A.T.N´Diaye et al, Structure of epitaxial graphene on Ir(111)*, New J. Phys.* **10**, 043033 (2008).

S2 A.T.N´Diaye et al, In situ observation of strain relaxation in epitaxial graphene*, New J. Phys.* **11**, 113056 (2009).

S3 D. Marchenko et al, Graphene for spintronics: giant Rashba splitting due to hybridization with gold. *Nature Communications* **3**, 1232 (2012).

S4 D. Ma, Z. Yang, First principles studies of Pb doping in graphene: stability, energy gap,and spin-orbit splitting*, New J. Phys.* **13**,123018 (2011).

S5 C. Weeks, J. Hu, J. Alicea, M. Franz, R. Wu, Engineering a Robust Quantum Spin Hall State in Graphene via Adatom Deposition, *Phys. Rev. X* **1**, 021001 (2011).

S6 P. San-Jose, J. Gónzalez, F. Guinea, Non-abelian Gauge Potential in Graphene bilayers, *Phys. Rev. Lett.*, **108**, 216802 (2012).

S7 G. Kresse and J. Hafner, Ab-initio molecular dynamics for liquid metals, *Phys. Rev*. B47, 558 (1993); G. Kresse and J. Furthmüller, Efficient iterative schemes for *ab initio* total-energy calculations using a plane wave basis set, *Phys. Rev*. B54, 11169 (1996); G. Kresse and D. Joubert, From ultrasoft pseudopotentials to the projector augmented-wave method, *Phys. Rev*. B59, 1758 (1999).

S8 P. E. Blöchl, Projector Augmented Wave method, *Phys. Rev.* B50, 17953 (1994).

S9 J. P. Perdew, K. Burke, and M. Ernzerhof, Generalized Gradient approximation made simple, *Phys. Rev. Lett.* 77, 3865 (1996).

S10 D. D. Koelling and B. N. Harmon, A technique for relativistic spin-polarised calculations, J. Phys. C: Sol. St. Phys. 10, 3107 (1977).

S11 F. Guinea, M.I. Katsnelson, A.K. Geim, Energy gaps and a zero-field quantum Hall effect in graphene by strain engineering, *Nature Phys.* **6**, 30 (2010).

S12 B.A. Bernevig, S.-C. Zhang, Quantum Spin Hall Effect, *Phys. Rev. Lett.* **96**, 106401 (2006).

S13 C.L. Kane, E.J. Mele, Quantum Spin Hall Effect in Graphene, *Phys. Rev. Lett.* **95**, 226801 (2005).